

# High-Voltage-Driven Surface Structuring and Electrochemical Stabilization of Ni-Rich Layered Cathode Materials for Li Rechargeable Batteries

Seok Hyun Song, Moses Cho, Inchul Park, Jong-Gyu Yoo, Kyung-Tae Ko, Jihyun Hong, Jongsoon Kim, Sung-Kyun Jung, Maxim Avdeev, Sungdae Ji, Seongsu Lee, Joona Bang, and Hyungsub Kim\*

Layered lithium–nickel–cobalt–manganese oxide (NCM) materials have emerged as promising alternative cathode materials owing to their high energy density and electrochemical stability. Although high reversible capacity has been achieved for Ni-rich NCM materials when charged beyond 4.2 V versus Li<sup>+</sup>/Li, full lithium utilization is hindered by the pronounced structural degradation and electrolyte decomposition. Herein, the unexpected realization of sustained working voltage as well as improved electrochemical performance upon electrochemical cycling at a high operating voltage of 4.9 V in the Ni-rich NCM LiNi<sub>0.895</sub>Co<sub>0.085</sub>Mn<sub>0.02</sub>O<sub>2</sub> is presented. The improved electrochemical performance at a high working voltage at 4.9 V is attributed to the removal of the resistive Ni<sup>2+</sup>O rock-salt surface layer, which stabilizes the voltage profile and improves retention of the energy density during electrochemical cycling. The manifestation of the layered Ni<sup>2+</sup>O rock-salt phase along with the structural evolution related to the metal dissolution are probed using in situ X-ray diffraction, neutron diffraction, transmission electron microscopy, and X-ray absorption spectroscopy. The findings help unravel the structural complexities associated with high working voltages and offer insight for the design of advanced battery materials, enabling the realization of fully reversible lithium extraction in Ni-rich NCM materials.

## 1. Introduction

The development of rechargeable Li-ion batteries (LIBs) with high energy density is becoming increasingly important as their application has extended from small portable electronic devices to electric vehicles (EVs) and grid-scale energy storage systems (ESSs).<sup>[1,2]</sup> Current LIBs still do not yet meet the requirements for automotive applications; thus, tremendous efforts have been focused on developing electrode materials with higher reversible capacities.<sup>[3–5]</sup> Layered transition metal oxide materials, namely LiCoO<sub>2</sub> (LCO), have received significant attention owing to their high energy density and theoretical capacity (≈272 mAh g<sup>-1</sup>) compared with those of commercially available cathodes, specifically spinel (≈148 mAh g<sup>-1</sup>) and olivine (≈170 mAh g<sup>-1</sup>) compounds.<sup>[6–10]</sup> However, Li-ion extraction is not fully reversible in LCO, resulting in a small practical capacity (≈140 mAh g<sup>-1</sup>). In the

S. H. Song, Dr. M. Cho, Dr. S. Ji, Dr. S. Lee, Dr. H. Kim  
Neutron Science Center  
Korea Atomic Energy Research Institute (KAERI)  
111 Daedeok-daero 989 Beon-Gil, Yuseong-gu  
Daejeon 34057, Republic of Korea  
E-mail: hyungsubkim@kaeri.re.kr

S. H. Song, Prof. J. Bang  
Department of Chemical and Biological Engineering  
Korea University  
145 Anam-Ro, Seongbuk-Gu, Seoul 02841, Republic of Korea

Dr. I. Park  
Battery Materials Research Center  
Research Institute of Industrial Science & Technology (RIST)  
67 Cheongam-ro, Pohang 37673, Republic of Korea

J.-G. Yoo, Dr. K.-T. Ko  
Max Planck POSTECH/Hsinchu Center for Complex Phase Materials  
67 Cheongam-ro, Pohang 37673, Republic of Korea

J.-G. Yoo, Dr. K.-T. Ko  
Department of Physics  
Pohang University of Science and Technology  
67 Cheongam-ro, Pohang 37673, Republic of Korea

 The ORCID identification number(s) for the author(s) of this article can be found under <https://doi.org/10.1002/aenm.202000521>.

DOI: 10.1002/aenm.202000521

Dr. K.-T. Ko  
Research Center for Materials Analysis  
Korea Basic Science Institute (KBSI)  
169-148 Gwahak-ro, Yuseong-gu, Daejeon 34133, Republic of Korea

Dr. J. Hong  
Center for Energy Materials Research  
Korea Institute of Science and Technology (KIST)  
5 Hwarang-ro 14 Gil, Seongbuk-gu, Seoul 02792, Republic of Korea

Prof. J. Kim  
Department of Nanotechnology and Advanced Materials Engineering  
Sejong University  
209 Neungdong-ro, Gwangjin-gu, Seoul 05006, Republic of Korea

Dr. S.-K. Jung  
Next Generation Battery Lab  
Material Research Center  
Samsung Advanced Institute of Technology (SAIT)  
Samsung Electronics Co., Ltd. 130 Samsung-ro, Yeongtong-gu, Suwon-si  
Gyeonggi-do 16678, Republic of Korea

Dr. M. Avdeev  
Australian Nuclear Science and Technology Organisation (ANSTO)  
New Illawarra Rd, Lucas Heights, NSW 2232, Australia

search for high-capacity cathodes, materials composed of Ni, Co, and Mn, known as  $\text{LiNi}_x\text{Co}_y\text{Mn}_{1-x-y}\text{O}_2$  (NCM) materials, have been extensively studied because of their higher capacity than that of LCO and their use of low cost elements of Ni and Mn.<sup>[11,12]</sup>  $\text{LiNi}_{0.33}\text{Co}_{0.33}\text{Mn}_{0.33}\text{O}_2$  and  $\text{LiNi}_{0.5}\text{Co}_{0.2}\text{Mn}_{0.3}\text{O}_2$  (NCM523) have been successfully commercialized owing to their advanced electrochemical performance and stability.

Recently, Ni-rich NCM ( $x \geq 0.8$ ) materials have been considered promising cathodes for application in mid- and large-scale ESSs because of their high reversible capacity of  $\approx 200 \text{ mAh g}^{-1}$ .<sup>[13,14]</sup> Nevertheless, there are several issues associated with these materials, including i) difficulties in synthesizing stoichiometric Ni-rich NCM because of the instability of  $\text{Ni}^{3+}$  during high-temperature synthesis, ii) the chemical instability of  $\text{Ni}^{4+}$  under highly delithiated conditions resulting in the formation of a resistive layer of  $\text{Ni}^{2+}\text{O}$  on the cathode surface, iii) oxygen release from the host structure, and iv) the generation of microcracks in the bulk from repeated Li-ion de/intercalation.<sup>[15–23]</sup> In addition, with increasing Ni content, more cation mixing between Ni and Li ions occurs during electrochemical cycling due to the similarly sized  $\text{Ni}^{2+}$  (0.69 Å) and  $\text{Li}^+$  (0.76 Å) ions, and the intermixing creates a more resistant layer on the surface, making the structure more unstable.<sup>[24–27]</sup> Although the reversible capacity has been dramatically increased in Ni-rich NCM materials, complete lithium extraction from NCM electrodes remains a great challenge because operating at high cut-off voltage leads to irreversible structural transition and electrolyte decomposition, resulting in safety issues and poor cycle performance.<sup>[17,28,29]</sup>

One of the issues remaining for Ni-rich NCM materials is identification of the descriptors affecting the irreversible capacity loss and voltage fade problems and their link to structural evolution upon gradual Li extraction at high operating voltage.<sup>[17,30,31]</sup> Although extensive work has been performed to resolve these issues and to highlight important insights regarding structural aspects, much of the work has focused on developing NCM electrodes with high Ni content and their synthesis and structural modification.<sup>[32]</sup> A few studies have offered insight into the structural characteristics at high voltage; for example, phase transition from the layered to spinel (Fd-3m) and rock-salt (Fm-3m) structure was observed in NCM materials, where the irreversibility of Li was more pronounced, resulting in voltage and capacity loss.<sup>[17,29]</sup> A recent study demonstrated the unexpectedly improved cycle performance at high voltage (4.8 V) in the LCO system, where the high voltage induced the dissolution of the resistive layer (spinel, rock-salt) and its reversal to its pristine form (rhombohedral (R-3m) layer), signifying the role of high working voltage on surface structuring during electrochemical cycling.<sup>[33]</sup> However, even though these studies have shown the effect of high voltage on cathode systems, the formation mechanism of resistive layers has not yet been revealed, and in-depth interpretation of the role of the amount of Li extracted in Ni-rich NCM and its correspondence to structural evolution at high voltage remains elusive. Thus, thorough analysis and quantification of structural parameters that affect the structural evolution of the resistive layer with the gradual extraction of Li for high-voltage electrochemistry is critical for further development of cathode materials.

In this study, we demonstrate the active role of the working voltage in determining the structural change of the surface resistive layer for the first time in Ni-rich NCM materials by using a combination of different analytical techniques, including X-ray diffraction (XRD), neutron diffraction (ND), transmission electron microscopy (TEM), and X-ray absorption spectroscopy (XAS). We reveal that the high-voltage operation of  $\text{LiNi}_{0.895}\text{Co}_{0.085}\text{Mn}_{0.02}\text{O}_2$  at 4.9 V induces the dissolution of the surface resistive layer, resulting in unexpected electrochemical stability compared with operation at 4.6 V, contradicting previous reports of higher charging voltages resulting in instability. This beneficial phenomenon was observed in other NCM materials of NCM523 and  $\text{LiNi}_{0.6}\text{Co}_{0.2}\text{Mn}_{0.2}\text{O}_2$  (NCM622) as well as in Ni-rich NCM. Our findings clarify the origin of the coupling between the working voltage and phase change of surface resistive layers, with the pronounced positive effects of electrochemistry at high voltage enabling new chemistry and mechanisms. With the physical/chemical insight provided in this study, full Li reversibility in Ni-rich NCM materials can be realized.

## 2. Results

### 2.1. Synthesis and Structural Characterization of $\text{LiNi}_{0.895}\text{Co}_{0.085}\text{Mn}_{0.02}\text{O}_2$

$\text{LiNi}_{0.895}\text{Co}_{0.085}\text{Mn}_{0.02}\text{O}_2$  was successfully synthesized using the conventional co-precipitation method followed by solid-state synthesis at 750 °C for 12 h with oxygen gas flow.<sup>[26]</sup> The crystal structure of  $\text{LiNi}_{0.895}\text{Co}_{0.085}\text{Mn}_{0.02}\text{O}_2$  was characterized by Rietveld refinement of the XRD and ND data, as shown in Figures S1 and S2, Supporting Information, confirming the well-defined rhombohedral  $\alpha\text{-NaFeO}_2$ -type layered structure (space group R-3m) with no trace of impurities.<sup>[3,15,34–36]</sup> The fitting was satisfactory with low reliability factors, and a summary of the crystal data is provided in Tables S1 and S2, Supporting Information. Rietveld refinement of the ND data revealed negligible cation mixing between  $\text{Li}_{\text{oct}}$  and  $\text{Ni}_{\text{oct}}$  (1.4%), which is in good agreement with previous reports of the crystal structure.<sup>[37,38]</sup> The scanning electron microscopy (SEM) images in Figure S3, Supporting Information confirm that the secondary particles of  $\text{LiNi}_{0.895}\text{Co}_{0.085}\text{Mn}_{0.02}\text{O}_2$  exhibited spherical morphology with a uniform size of approximately 10  $\mu\text{m}$ . The size of the primary particles was determined to be 100–200 nm.

### 2.2. Electrochemical Performance of $\text{LiNi}_{0.895}\text{Co}_{0.085}\text{Mn}_{0.02}\text{O}_2$

Figure 1a–c present the galvanostatic charge/discharge profiles of  $\text{LiNi}_{0.895}\text{Co}_{0.085}\text{Mn}_{0.02}\text{O}_2$  cycled at cut-off voltages of 4.25, 4.6, and 4.9 V versus  $\text{Li}^+/\text{Li}$ , respectively. The electrode delivered an initial discharge capacity of 210  $\text{mAh g}^{-1}$  at a cut-off voltage of 4.25 V, and the capacity slightly increased to 222 and 230  $\text{mAh g}^{-1}$  upon increasing the cut-off voltage to 4.6 and 4.9 V, respectively. A sloppy discharge profile attributed to an additional capacity of 10–20  $\text{mAh g}^{-1}$  was observed above 4.25 V (marked by the dotted circle in Figure 1b,c), indicating the extended reversible Li de/intercalation in a higher voltage window. The discharge capacity decreased with prolonged

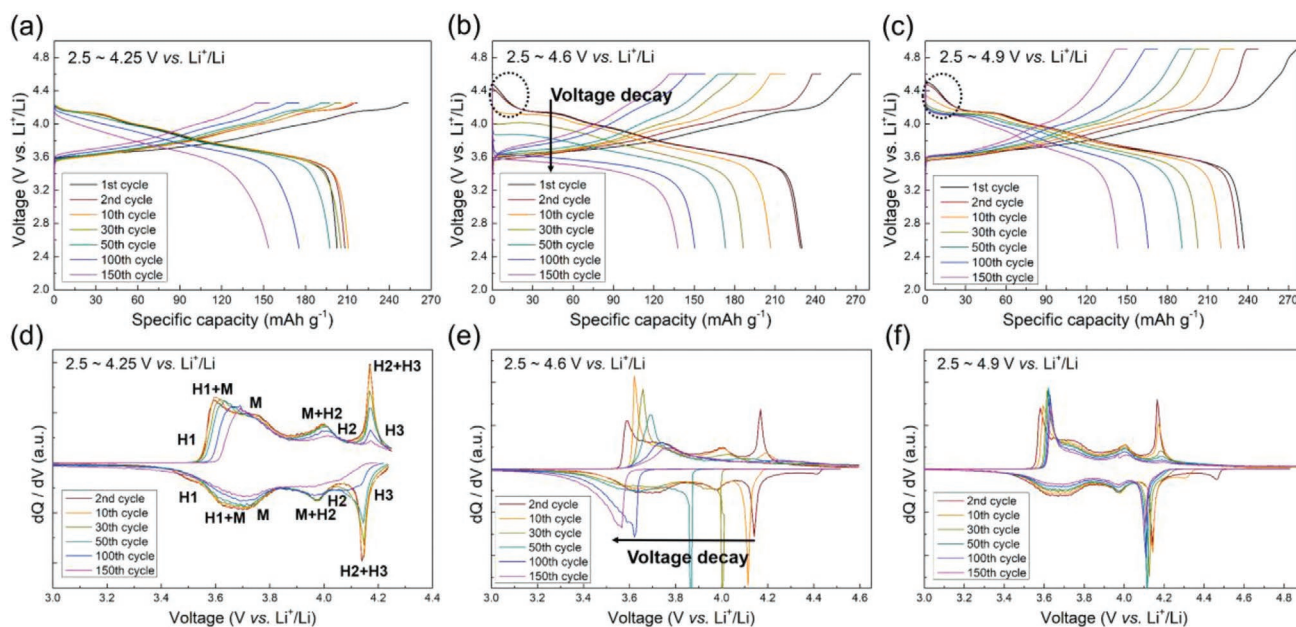


**Figure 1.** Galvanostatic charge/discharge profiles of  $\text{LiNi}_{0.895}\text{Co}_{0.085}\text{Mn}_{0.02}\text{O}_2$  at cut-off voltages of a) 4.25 V, b) 4.6 V, and c) 4.9 V versus  $\text{Li}^+/\text{Li}$ .  $dQ/dV$  plots of  $\text{LiNi}_{0.895}\text{Co}_{0.085}\text{Mn}_{0.02}\text{O}_2$  at cut-off voltages of d) 4.25 V, e) 4.6 V, and f) 4.9 V versus  $\text{Li}^+/\text{Li}$ .

cycling, demonstrating the irreversibility of the Li extraction regardless of the voltage cut-off. Nonetheless, the electrode exhibited different discharge profiles at each cut-off voltage upon electrochemical cycling, which could be further elaborated. The capacity of the electrode cycled at a cut-off voltage of 4.25 V was well maintained up to 30 cycles and then decreased rapidly. The  $dQ/dV$  plot in Figure 1d shows the sequential phase transition (H1–M–H2–H3), where the original layered structure (H1) transformed to the monoclinic phase (M) at 3.6 V, hexagonal phase (H2) at 3.9 V, and another hexagonal phase (H3) at 4.15 V.  $\text{LiNi}_{0.895}\text{Co}_{0.085}\text{Mn}_{0.02}\text{O}_2$  suffered from structural instability of H3 owing to large anisotropic lattice volume changes, as observed in  $\text{LiNiO}_2$ , resulting in cracks and hindering Li re-intercalation into the system.<sup>[21,39,40]</sup> As a result, the H2–H3 phase transition peak disappeared between the 100th and 150th cycles, indicating permanent capacity lost. At 4.6 V, significant capacity and voltage decay were observed after 10 cycles (Figure 1b,e), with the simultaneous capacity loss and voltage decay confirmed upon long cycling at high voltage in the cathodes, as suggested by previous studies.<sup>[17,26,29]</sup> A substantial voltage shift was observed upon electrochemical cycling, and an overpotential of  $\approx 0.6$  V was confirmed after 150 cycles. The long cycling test triggered structural breakdown, resulting in the large polarization. Strikingly, the capacity and voltage decay were alleviated in the cell cycled at the higher voltage of 4.9 V, as shown in Figure 1c,f. Contrary to the general belief that high-voltage operation of Ni-rich NCM electrode materials results in large structural change and surface degradation, the cell cycled at a cut-off voltage of 4.9 V exhibited more stable capacity and voltage retention upon electrochemical cycling.<sup>[17,29]</sup> Although the reduction of the capacity proceeded faster than that for the 4.25 V cut-off voltage, the voltage profile above 4.0 V (in the H2–H3 phase transition region) remained more stable than that in the cells cycled at 4.6 and 4.25 V up to 150 cycles.

The gravimetric energy density plot in Figure S4, Supporting Information further confirms the enhanced cycle performance of the cell cycled at 4.9 V. The initial energy densities for the cells cycled at 4.6 and 4.9 V were similar ( $\approx 900$  Wh  $\text{kg}^{-1}$ ); however, more severe reduction of the energy density was observed for the cell cycled at a cut-off voltage of 4.6 V.

### 2.3. Crystal Structural Change of $\text{LiNi}_{0.895}\text{Co}_{0.085}\text{Mn}_{0.02}\text{O}_2$ During Charge/Discharge

To understand the structural evolution of  $\text{LiNi}_{0.895}\text{Co}_{0.085}\text{Mn}_{0.02}\text{O}_2$  upon battery cycling, in situ XRD analyses during the initial cycle were conducted. The (003) peak in Figure 2a underwent a continuous peak shift to lower  $2\theta$  angle during the initial charge process, and the sequential H1–M–H2–H3 structural transition occurred with increasing voltage up to 4.25 V, which is consistent with previous findings.<sup>[15,26,35]</sup> The peak returned to the initial  $2\theta$  position during the subsequent discharge reaction, indicating that the charge/discharge reaction is reversible. Further charge up to 4.6 and 4.9 V resulted in an additional peak shift to higher  $2\theta$  angle, which originated from contraction of the  $c$ -lattice parameter, as shown in Figure 2b,c. The (110) peak underwent a continuous shift to higher  $2\theta$  angles during charge up to 4.25 V, and the peak shifted to lower angle following charge up to 4.6 and 4.9 V. Figure 2d–f present the galvanostatic charge/discharge profiles and change of lattice parameter values during the first cycle at cut-off voltages of 4.25, 4.6, and 4.9 V, respectively. A continuous change of the lattice parameters was observed during charge up to 4.1 V, with the  $c$ -lattice parameter increasing and the  $a$ -lattice parameter decreasing during the phase transition from the H1 to H2 phase. A notable structural change was observed in the highly delithiated state above 4.1 V, where the H2 and H3

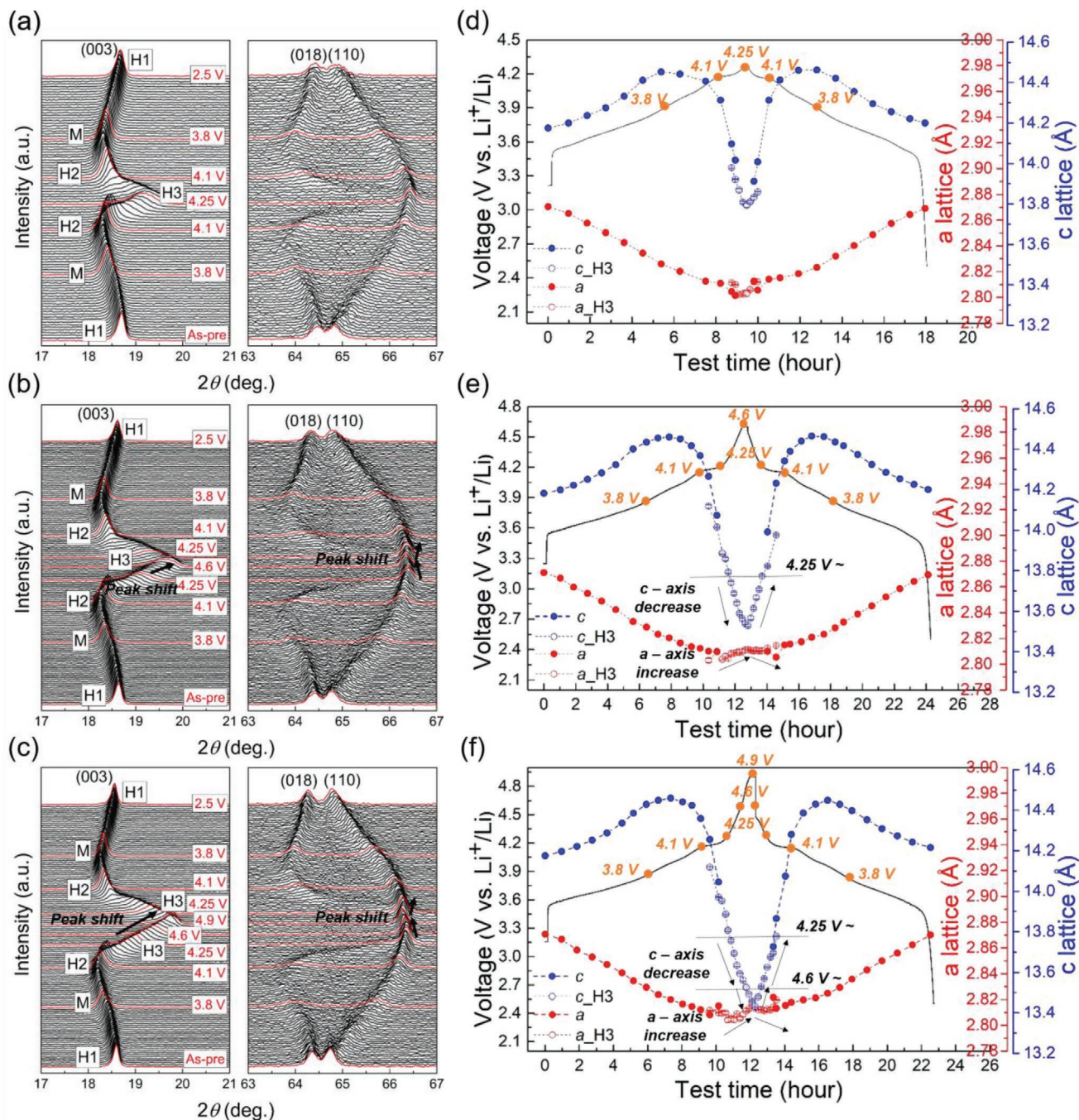


**Figure 2.** In situ XRD patterns of  $\text{LiNi}_{0.895}\text{Co}_{0.085}\text{Mn}_{0.02}\text{O}_2$  during initial electrochemical cycling at cut-off voltages of a) 4.25 V, b) 4.6 V, and c) 4.9 V versus  $\text{Li}^+/\text{Li}$ .  $a$ - and  $c$ -lattice parameter changes of electrodes with cut-off voltages of d) 4.25 V, e) 4.6 V, and f) 4.9 V versus  $\text{Li}^+/\text{Li}$ .

phase transition occurs. A large contraction of the  $c$ -lattice parameter occurred during the charging process from 4.1 to 4.25 V. Further charge up to 4.6 and 4.9 V resulted in collapse of the  $c$ -lattice parameter and slight expansion of the  $a$ -lattice parameter, resulting in anisotropic volume changes (Figure 2e,f). These findings indicate that the additional capacity above 4.25 V is rooted in the solid-solution reaction of the H3 phase and not in electrolyte decomposition or the oxygen redox reaction. The reversible structural transition was confirmed until

the fifth cycle by in situ XRD analysis, as shown in Figure S5, Supporting Information.

#### 2.4. Structural Change of $\text{LiNi}_{0.895}\text{Co}_{0.085}\text{Mn}_{0.02}\text{O}_2$ Upon Electrochemical Cycling

Figure 3a presents XRD patterns of the pristine electrode and electrodes cycled at cut-off voltages of 4.25, 4.6, and

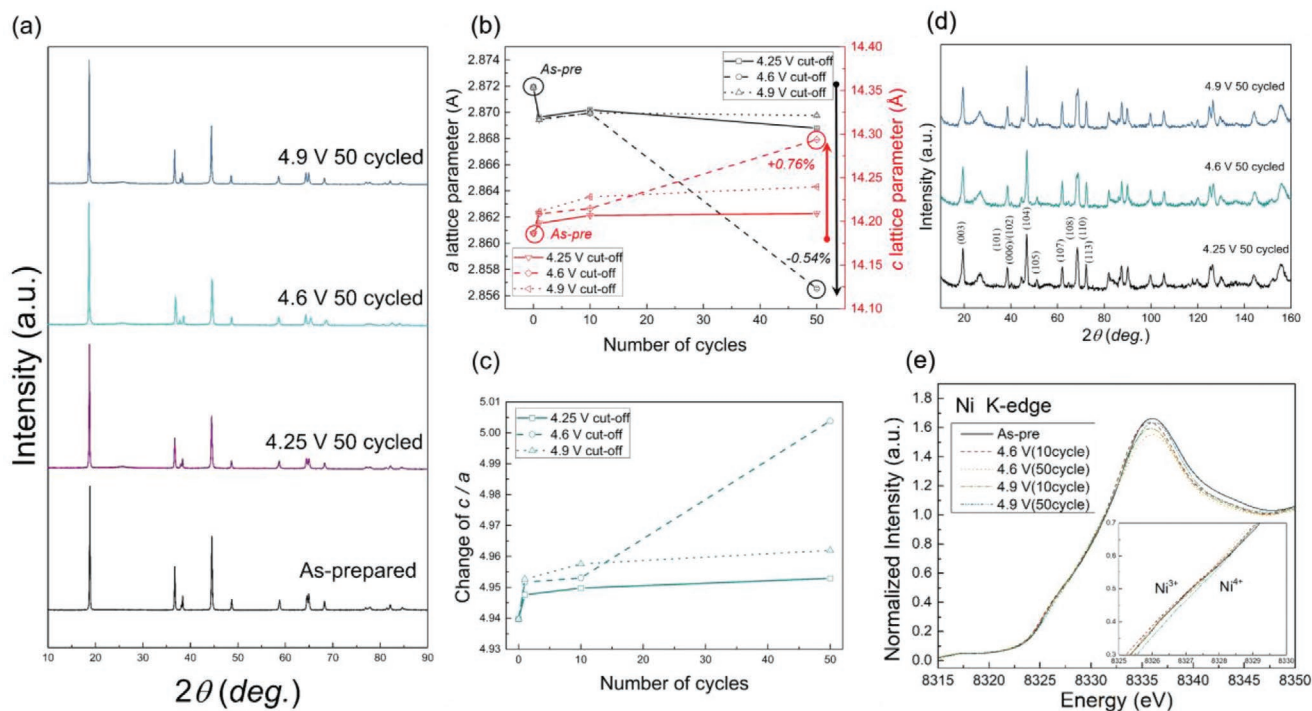


**Figure 3.** XRD patterns of  $\text{LiNi}_{0.895}\text{Co}_{0.085}\text{Mn}_{0.02}\text{O}_2$  cycled at a) 4.25, 4.6, and 4.9 V versus  $\text{Li}^+/\text{Li}$ . Changes in the b) lattice parameters and c) the ratio of  $c/a$  of  $\text{LiNi}_{0.895}\text{Co}_{0.085}\text{Mn}_{0.02}\text{O}_2$  upon electrochemical cycling at each cut-off voltage. d) ND patterns of  $\text{LiNi}_{0.895}\text{Co}_{0.085}\text{Mn}_{0.02}\text{O}_2$  after 50 cycles at 4.25, 4.6, and 4.9 V versus  $\text{Li}^+/\text{Li}$ . e) Ni K-edge XANES spectra of  $\text{LiNi}_{0.895}\text{Co}_{0.085}\text{Mn}_{0.02}\text{O}_2$  cycled at 4.6 and 4.9 V versus  $\text{Li}^+/\text{Li}$ .

4.9 V versus  $\text{Li}^+/\text{Li}$ , respectively. The crystal structure of  $\text{LiNi}_{0.895}\text{Co}_{0.085}\text{Mn}_{0.02}\text{O}_2$  was well maintained after electrochemical cycling up to 50 cycles, with no traces of crystalline spinel or rock-salt phases for the cycled electrodes at any of the cut-off voltages. Clear shifts of the (003), (018), and (110) peaks upon electrochemical cycling were observed, with the (003) and (018) peaks shifting to lower  $2\theta$  angles and the (110) peak shifting to higher  $2\theta$  angles, as shown in Figure S6, Supporting Information. Interestingly, the largest shifts in the (003) and (110) peaks were observed in the XRD pattern of the electrode after 50 cycles at 4.6 V, suggesting that electrochemical cycling at 4.6 V is the most irreversible process. The lattice parameter changes upon electrochemical cycling observed in Figure 3b,c and Figure S7, Supporting Information indicate the anisotropic variation of the lattice parameters and unit-cell volume as cycling progressed. The  $a$ -lattice parameter decreased by  $\approx 0.08\%$  after 1 cycle with a cut-off voltage of 4.25 V, whereas the  $c$ -lattice parameter showed a 0.08% increase. The small lattice parameter changes were confirmed upon repeated electrochemical cycling up to 50 cycles, where the  $a$ -lattice parameter decreased by  $\approx 0.11\%$  and the  $c$ -lattice parameter increased by  $\approx 0.16\%$  after 50 cycles. At 4.6 V cut-off conditions, significant cell parameter changes were observed, with the  $a$ -lattice parameter decreasing by approximately 0.54% and the  $c$ -lattice parameter increasing by approximately 0.76% after 50 cycles. This finding is consistent with the largest shift of the (003) peak to the left and of the (110) peak to the right in Figure S6, Supporting Information. Note that the lattice parameter changes of the electrode cycled at 4.9 V were smaller than those of the electrode cycled at 4.6 V. The  $a$ -lattice parameter decreased

by  $\approx 0.07\%$  and the  $c$ -lattice parameter increased by  $\approx 0.37\%$  after 50 cycles (Figure 3b). In addition, a larger lattice volume change was confirmed for the electrode cycled at 4.6 V ( $\approx 0.32\%$ ) compared with those of the electrodes cycled at 4.25 ( $\approx 0.059\%$ ) and 4.9 V ( $\approx 0.22\%$ ), as shown in Figure S7, Supporting Information. The  $c/a$  ratio which can be regarded as an indicator in determining the anisotropic structural changes of layered materials shown in Figure 3c illustrates that the greatest anisotropic expansion occurs from the electrode cycled at 4.6 V.<sup>[15]</sup> All of the  $c/a$  values for the cycled electrodes are provided in the Supporting Information (Table S3, Supporting Information). These findings further confirm that electrochemical cycling of  $\text{LiNi}_{0.895}\text{Co}_{0.085}\text{Mn}_{0.02}\text{O}_2$  at a cut-off voltage of 4.6 V causes the largest permanent structural disorder. In contrast, the suppressed lattice contraction and expansion in the electrode cycled at 4.9 V hints at the possible positive high-voltage effects, as demonstrated in earlier studies on the LCO system.<sup>[33]</sup> The structural disorder in the electrode attributed to the atomic disorder or lattice strain is further confirmed by the Williamson-Hall plot in Figure S8, Supporting Information. An increase of the slope, indicating an increase in the amount of microstrain, was observed from the electrode after electrochemical cycling at a cut-off voltage of 4.25 V (Figure S8a, Supporting Information), and the slope was maintained up to 50 cycles. A significant increase of the slope was observed for the electrode cycled at 4.6 V, as shown in Figure S8b, Supporting Information. This finding indicates that the strain originating from the structure disorder continues to increase as the cycle number increases. However, there was almost no change for the electrode cycled at a cut-off voltage of 4.9 V (Figure S8c, Supporting Information).

To quantify the structural disorder in cycled electrode samples of  $\text{LiNi}_{0.895}\text{Co}_{0.085}\text{Mn}_{0.02}\text{O}_2$ , ND experiments were conducted. The ND patterns in Figure 3d show that the crystal structure of the cycled electrodes was well maintained after 50 cycles, with no trace of diffraction peaks from spinel or rock-salt structures and broad carbon peaks detected at low  $2\theta$  angles of approximately  $30^\circ$ . The lattice parameters, atomic positions, and occupancies were analyzed by Rietveld refinement, and the results are presented in Figure S9, Supporting Information and Table S4, Supporting Information. For the Rietveld refinement analysis, the Li, Ni, Co, and Mn contents were determined by inductively coupled plasma mass spectrometry (ICP-MS) analysis in advance, with the results presented in Table S5, Supporting Information. After 50 cycles, the Li content in the crystal structure of each cycled electrode was determined to be lower than the initial content, which may have resulted from structural degradation and capacity decay. Approximately 93% of Li was recovered after 50 cycles at a cut-off voltage of 4.25 V, whereas 83% and 85% of Li were recovered from the electrodes cycled at 4.6 and 4.9 V, respectively. Interestingly, the largest structural change was confirmed for the electrode cycled at 4.6 V rather than that at the higher voltage of 4.9 V. First, the largest lattice contraction along the  $a$ -axis and expansion along the  $c$ -axis were observed for the cycled electrode at 4.6 V, which is consistent with the XRD analyses. The  $a$ -lattice parameter decreased from 2.87186 (7) Å to 2.8630 (2) Å while the  $c$ -lattice parameter increased from 14.1862 (4) Å to 14.211 (2) Å after battery cycling. Furthermore, the electrode cycled at a cut-off voltage of 4.6 V exhibited the largest contraction of bond lengths between transition metal and oxygen ions ( $\approx 0.64\%$ ) and the largest expansion of bond lengths between Li and oxygen ions ( $\approx 0.45\%$ ) after 50 cycles. Note that a large amount ( $\approx 3.8\%$ ) of Ni in the transition metal layer ( $\text{Ni}_{\text{oct}}$ ) migrated to octahedral sites in the Li layer ( $\text{Li}_{\text{oct}}$ ) after electrochemical cycling at a cut-off voltage of 4.6 V, whereas negligible migration was observed for the electrodes cycled at 4.25 and 4.9 V. The transition metal migration in layered-type NCM materials has been considered an origin of phase transition from layered to spinel or rock-salt phases and has been previously investigated using TEM and XAS analyses.<sup>[41–47]</sup> It has been observed that transition

metals migrate from octahedral sites in the transition metal layer to octahedral or tetrahedral sites in the lithium layer at highly charged states, and the subsequent segregation of transition metals in the lithium layer triggers the phase transition from layered to spinel or rock-salt structures. We believe that the increased Li–Ni intermixing and structural disorder at 4.6 V triggers the spinel and rock-salt formation on the particle surface and results in deterioration of the electrochemical performance upon repeated battery cycling.

The oxidation states of Ni and Co in the cycled samples were further examined using X-ray absorption near edge structure (XANES) analyses, as shown in Figure 3e. The Ni K-edge XANES spectra of the as-prepared and cycled electrode samples at 4.6 and 4.9 V show negligible differences, and a slight spectrum shift to higher energy was observed for the electrode after 50 cycles at 4.9 V. Similarly, there were no distinguishable differences in the Co K-edge XANES spectra, as shown in Figure S10, Supporting Information.

## 2.5. Surface Structural Characterization of Cycled Samples of $\text{LiNi}_{0.895}\text{Co}_{0.085}\text{Mn}_{0.02}\text{O}_2$

Structural characterization of the particle surface was performed using soft XAS and TEM analyses. Figure 4a–c show the  $L_2$  and  $L_3$ -edge XAS spectra of Ni after electrochemical cycling at 4.25, 4.6, and 4.9 V versus  $\text{Li}^+/\text{Li}$ . The oxidation state of Ni on the particle surface of the as-prepared  $\text{LiNi}_{0.895}\text{Co}_{0.085}\text{Mn}_{0.02}\text{O}_2$  was determined to be  $\text{Ni}^{3+}$  with a small amount of  $\text{Ni}^{2+}$ .<sup>[11,48–50]</sup> Interestingly, a large amount of  $\text{Ni}^{2+}$  was formed on the particle surface after one cycle regardless of the cut-off voltage, as observed in Figure 4a, where the peaks at the  $L_2$ - and  $L_3$ -edge shifted to lower energy, and the peak intensities at 854.4 and 871.1 eV decreased after one cycle. The reduction of the oxidation state of Ni from  $\text{Ni}^{3+}$  to  $\text{Ni}^{2+}$  is attributed to the phase transformation from layered  $\text{LiNi}_{0.895}\text{Co}_{0.085}\text{Mn}_{0.02}\text{O}_2$  to spinel and rock-salt phases.<sup>[51,52]</sup> Negligible changes in the spectra were observed until ten cycles, as shown in Figure 4b; however, a significant change occurred after 50 cycles. As cycling proceeded, a large amount of  $\text{Ni}^{2+}$  compounds such as spinel or rock-salt

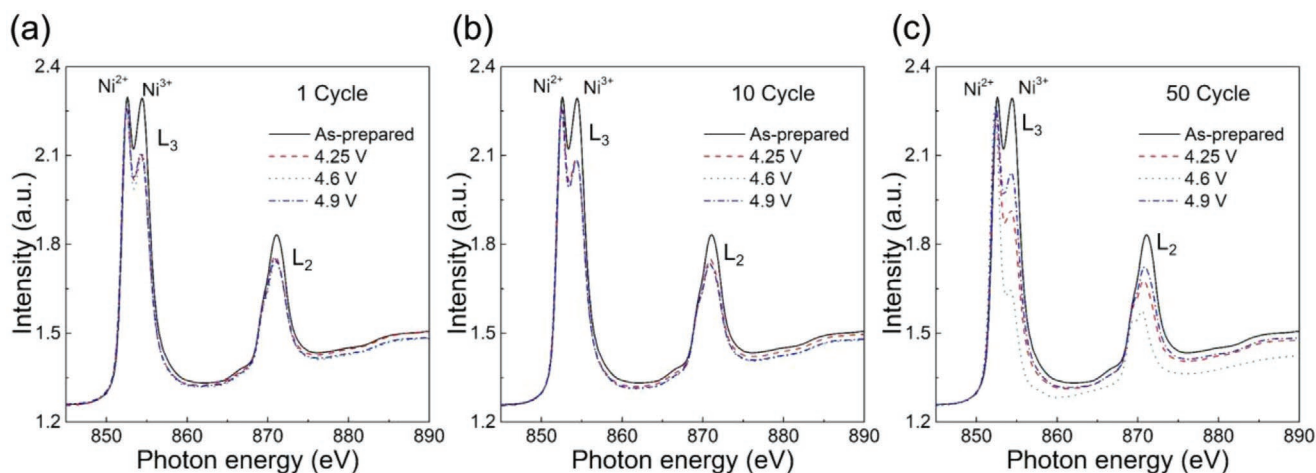


**Figure 4.** Ni L-edge XAS spectra of  $\text{LiNi}_{0.895}\text{Co}_{0.085}\text{Mn}_{0.02}\text{O}_2$  electrode after a) 1 cycle, b) 10 cycles, and c) 50 cycles at 4.25, 4.6, and 4.9 V versus  $\text{Li}^+/\text{Li}$ .

phases were gradually formed on the particle surface due to the transition metal migration and subsequent segregation. The XAS spectra of Ni shown in Figure 4c indicate that large amounts of  $\text{Ni}^{2+}$  were detected after 50 cycles at each cut-off voltage. Surprisingly, the smallest amount of  $\text{Ni}^{2+}$  was detected for the sample cycled at the highest voltage of 4.9 V, whereas the largest amount of  $\text{Ni}^{2+}$  was detected for the electrode cycled at 4.6 V. Furthermore, the  $\text{Ni}^{2+}$  content in the electrode cycled at 4.9 V was much lower than that cycled at 4.25 V. The following phenomenon was further confirmed with Co L-edge XAS spectra shown in Figure S11, Supporting Information.

Extensive high-resolution-TEM (HR-TEM) analyses were performed to estimate where the phase transformation occurs. TEM and fast Fourier transformed (FFT) images of the as-prepared electrodes and electrodes after ten cycles at each cut-off voltage are presented in Figure S12, Supporting Information. Only the layered phase was observed in all the samples, indicating that mild phase change occurs until the tenth cycle under all conditions, which is in a good agreement with the XAS results. **Figure 5a** presents TEM and FFT images of the electrode after 50 cycles at 4.25 V. The layered and spinel phases coexisted in the inner (region 1) and outer (region 2) surface regions, which is consistent with previous findings.<sup>[17]</sup> The d-spacings obtained from the lattice images are  $\approx 2.44$  and  $\approx 1.42$  Å, which can be matched with the (101) plane, representing the layered, and the (110), (044) plane representing the layered, spinel phase, respectively. Note that the rock-salt phase, which can be indexed as the (111) plane with a d-spacing of 2.41 Å, was observed on the particle surface (region 2) of the electrode after 50 cycles at a cut-off voltage of 4.6 V, whereas layered and spinel phases coexisted in the inner region (region 1), which is consistent with the Ni L-edge XAS spectra (Figure 5b).<sup>[50,53–58]</sup> The thickness of the cubic region was determined to be  $\approx 10$  nm from FFT analysis. However, the cubic phase was not detected on the particle surface of the electrode after 50 cycles at 4.9 V, where the only layered and spinel phases were observed from the inner and outer region, as shown in Figure 5c. Note that the surface structure of the electrode cycled at 4.9 V remained much more stable despite the voltage being above 4.6 V. We speculate that this stability mainly originates from the dissolution of Ni at a specific high voltage over 4.6 V reported in previous studies.<sup>[23,33]</sup> Charging up to 4.6 V induces the transition metal migration, resulting in resistive spinel and rock-salt formation on the particle surface; however, at certain voltages above 4.6 V, the resistive layer is observed to dissolve, leaving only the original layer.

The electrochemical impedance spectroscopy (EIS) results presented in Figure S13, Supporting Information further support the surface stabilization of the electrode at the high voltage of 4.9 V. The charge-transfer resistance ( $R_{\text{ct}}$ ), corresponding to the second semicircle in Figure S13b,c, Supporting Information, increased as the cycle number increased, which resulted from structural deformation of the particle surface of  $\text{LiNi}_{0.895}\text{Co}_{0.085}\text{Mn}_{0.02}\text{O}_2$  during repeated battery cycling.<sup>[25,59]</sup> Interestingly, the highest  $R_{\text{ct}}$  value was observed from the electrode after 30 cycles at a cut-off voltage of 4.6 V, indicating that more structural deformation occurred for the electrode cycled at 4.6 V than for those cycled at 4.25 and 4.9 V.  $R_{\text{ct}}$  increased from 40.12 to 130723 Ω after 30 cycles at

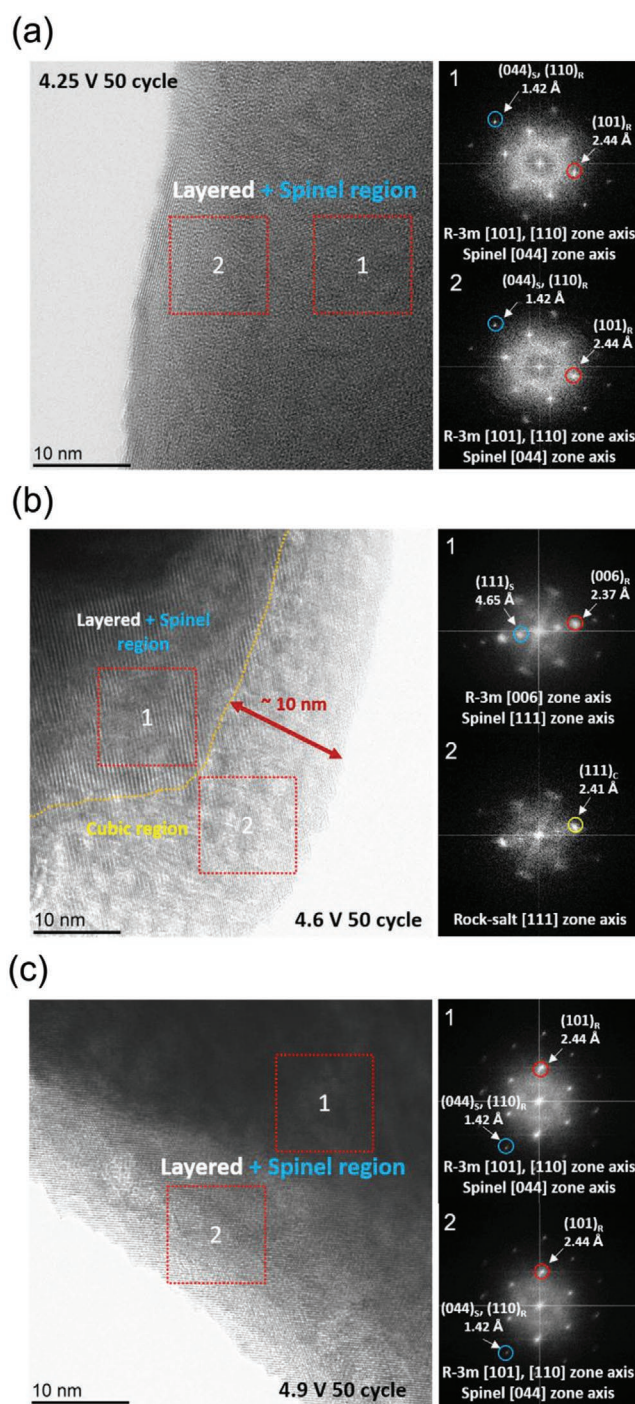


**Figure 5.** TEM and FFT images of  $\text{LiNi}_{0.895}\text{Co}_{0.085}\text{Mn}_{0.02}\text{O}_2$  electrode after 50 cycles at a) 4.25, b) 4.6, and c) 4.9 V versus  $\text{Li}^+/\text{Li}$ .

4.6 V and to 1123.06 Ω after 30 cycles at 4.9 V. In addition,  $R_{\text{ct}}$  of the cycled electrode at cut-off voltages of 4.25 and 4.6 V continuously increased from 10 to 30 cycles, whereas it decreased at the 4.9 V cut-off condition. These findings indicate that the surface structure is stabilized at 4.9 V. All of the resistance values are provided in the Supporting Information (Table S6, Supporting Information). Time-of-flight secondary-ion mass spectrometry (TOF-SIMS) analysis was further performed

to characterize the solid–electrolyte interphase (SEI) layer, which may be formed on the surface of the electrode at high voltages, as shown in Figure S14, Supporting Information. The components of  $\text{LiF}_2^-$ ,  $\text{C}_2\text{HO}^-$ ,  $\text{C}_2\text{F}^-$ , and  $\text{POF}_2^-$ , which are commonly observed from the SEI layer, were detected for all of the cycled electrodes, and the amounts of impurities were similar for the three cut-off voltage conditions.<sup>[15]</sup> Therefore, taken together, the surface stabilization at a specific high cut-off voltage of 4.9 V occurs because of the dissolution of the  $\text{Ni}^{2+}\text{O}$  like resistive layer, not the effect of organic impurities.

### 3. Discussion

Figure 6a presents a schematic representation of the structural change of  $\text{LiNi}_{0.895}\text{Co}_{0.085}\text{Mn}_{0.02}\text{O}_2$  during battery cycling. Upon repeated electrochemical cycling in the voltage range of

2.5–4.25 V versus  $\text{Li}^+/\text{Li}$ , the layered phase gradually transformed into a spinel phase as a result of the transition metal migration and subsequent segregation. A large amount of spinel phase formed on the particle surface after 50 cycles. Electrochemical cycling at high voltage of 4.6 V resulted in more rapid formation of the spinel and rock-salt phases on the particle surface because of the increased amount of highly reactive  $\text{Ni}^{4+}$ , which induced severe structural change, including *c*-lattice parameter collapse and transition metal migration, resulting in voltage and capacity decay. This result is consistent with the finding of previous studies that the continuous formation of highly resistive surface layers consisting of spinel or rock-salt phases results in deterioration of the cycle performance of Ni-rich NCM materials during high-voltage battery cycling.<sup>[15,19–23,26]</sup> Nonetheless, the electrode cycled at a cut-off voltage of 4.9 V exhibited superior capacity and voltage retention upon repeated battery cycling compared with the electrode cycled at 4.6 V. This finding is mainly attributed to

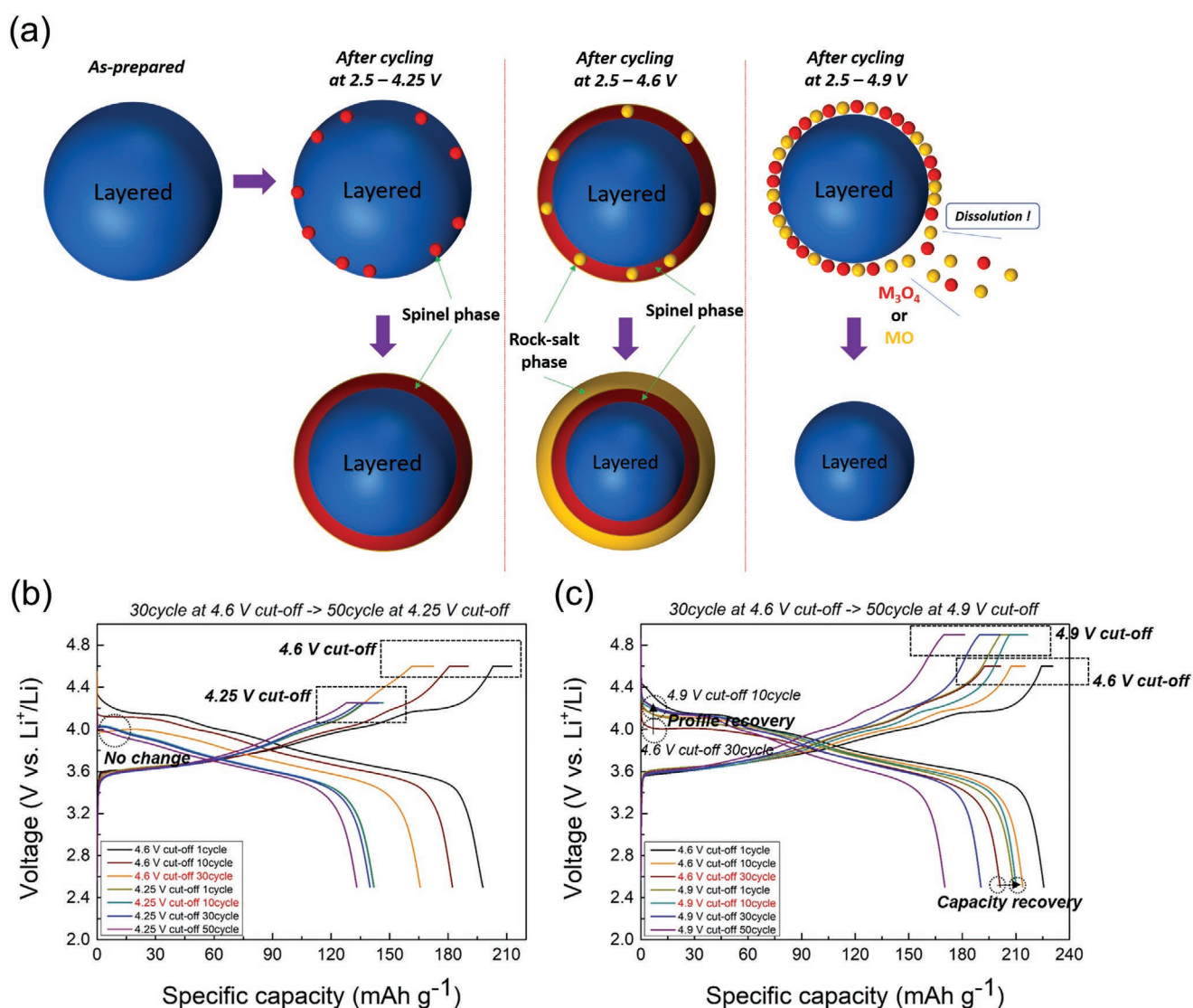


**Figure 6.** a) Schematic representation of structural evolution of  $\text{LiNi}_{0.895}\text{Co}_{0.085}\text{Mn}_{0.02}\text{O}_2$  upon high-voltage electrochemical cycling at 4.25, 4.6, and 4.9 V versus  $\text{Li}^+/\text{Li}$ . Galvanostatic charge/discharge profiles of  $\text{LiNi}_{0.895}\text{Co}_{0.085}\text{Mn}_{0.02}\text{O}_2$  after charge/discharge at a cut-off voltage of 4.6 V versus  $\text{Li}^+/\text{Li}$  for 30 cycles followed by charge/discharge at a cut-off voltage of b) 4.25 V and c) 4.9 V versus  $\text{Li}^+/\text{Li}$  for 50 cycles.

the continuous etching of the surface at a rate faster than the accumulation of the resistive rock-salt phase. The main dissolved component at high voltage was nickel, as confirmed by the ICP-MS and scanning electron microscopy–energy dispersive spectroscopy (SEM-EDS) results (Tables S5 and S7, Supporting Information).<sup>[23]</sup> The dissolution of the resistive layer at 4.9 V is beneficial for suppressing structural evolution and voltage decay upon repeated cycling, resulting in electrochemical stabilization.

To verify the favorable effect during high-voltage operation, we performed electrochemical tests using various cut-off voltages. The electrode was cycled under the 4.6 V cut-off condition for 30 cycles, followed by cycling under different cut-off conditions (4.25 and 4.9 V) for 50 cycles. The electrochemical cycling in the voltage range of 2.5–4.6 V led to significant voltage and capacity decay after 30 cycles. Upon the subsequent cycling at 4.25 V, neither the voltage profile nor capacity was recovered, as observed in Figure 6b, where the capacity decreased from 165 to 142 mAh g<sup>-1</sup>, and the voltage profile was maintained. However, upon cycling at 4.9 V after cycling at 4.6 V, both the voltage and capacity were recovered, as observed in Figure 6c. The specific capacity increased by approximately 10 mAh g<sup>-1</sup> after one cycle at 4.9 V, and the voltage profile gradually recovered to higher voltage as cycling proceeded. From these results, it is evident that the high-voltage operation at 4.9 V enhances the electrochemical performance by stabilizing the particle surface of the electrode. In addition, we discovered that similar electrochemical stabilization occurs at high voltages not only in LiNi<sub>0.895</sub>Co<sub>0.085</sub>Mn<sub>0.02</sub>O<sub>2</sub> but also in other NCM materials, as shown in Figures S15 and S16, Supporting Information. Suppressed voltage and capacity decay under high-voltage operation were observed for both NCM523 and NCM622 to different extents.

## 4. Conclusion

In summary, structural and electrochemical stabilization of Ni-rich NCM materials under high-voltage battery operation was revealed for the first time using XRD, ND, TEM, and XAS analyses. Our results reveal that high-voltage operation of LiNi<sub>0.895</sub>Co<sub>0.085</sub>Mn<sub>0.02</sub>O<sub>2</sub> at 4.9 V leads to dissolution of the surface resistive layer, which is beneficial for suppressing structural evolution and voltage decay upon repeated battery cycling. Although the high-voltage battery operation involves the loss of active materials due to continuous etching of the particle surface, the strategy of coating foreign matter on the surface may improve the electrochemical performance under high-voltage cycling. This study highlights the importance of surface engineering of Ni-rich NCM materials and provides insight for achieving full utilization of Li in NCM layered cathode materials.

## 5. Experimental Section

**Synthesis of LiNi<sub>0.895</sub>Co<sub>0.085</sub>Mn<sub>0.02</sub>O<sub>2</sub>:** LiNi<sub>0.895</sub>Co<sub>0.085</sub>Mn<sub>0.02</sub>O<sub>2</sub> powder was synthesized using the conventional solid-state method. Stoichiometric amounts of LiOH·H<sub>2</sub>O (99.995%, Sigma-Aldrich) and Ni<sub>0.895</sub>Co<sub>0.085</sub>Mn<sub>0.02</sub>(OH)<sub>2</sub> were carefully mixed by hand grinding to prevent particle breakage. The ground powder was pelletized under a pressure of 250 kg cm<sup>-2</sup> and heated at 750 °C for 12 h under O<sub>2</sub> gas

flow. The O<sub>2</sub> gas flow rate was 50–70 cc min<sup>-1</sup>. The resulting powder was collected from the furnace at 120 °C and transferred to an Ar-filled glove box to avoid moisture contamination.

**Structure Characterization of LiNi<sub>0.895</sub>Co<sub>0.085</sub>Mn<sub>0.02</sub>O<sub>2</sub>:** The crystal structures of the LiNi<sub>0.895</sub>Co<sub>0.085</sub>Mn<sub>0.02</sub>O<sub>2</sub> powder samples were characterized using ND and XRD analyses. Powder XRD data were obtained using an X-ray diffractometer (Empyrean, Malvern Panalytical) equipped with Cu K $\alpha$  radiation ( $\lambda = 1.540598 \text{ \AA}$ ). The measurement was conducted in the  $2\theta$  range of 10–90° with a step size of 0.013 and step time of 1 s. In situ charge/discharge XRD data were collected in the  $2\theta$  range of 10–80° with a step size of 0.026 and step time of 0.3 s. The measurement was performed using Swagelok-type cells with beryllium windows. ND data of LiNi<sub>0.895</sub>Co<sub>0.085</sub>Mn<sub>0.02</sub>O<sub>2</sub> was obtained from the HANARO facility at the Korea Atomic Energy Research Institute (KAERI). The measurement was conducted in the  $2\theta$  range of 0–180° with a step size of 0.05 using a constant wavelength of 1.834333 Å. ND experiments of ex situ powder samples of Li<sub>1-x</sub>Ni<sub>0.895</sub>Co<sub>0.085</sub>Mn<sub>0.02</sub>O<sub>2</sub> were performed using the Echidna machine at the OPAL facilities of the Australian Nuclear Science and Technology Organization (ANSTO). ND data were collected in the  $2\theta$  range of 0–163.95° with a step size of 0.05 using a constant wavelength of 1.6215 Å. The atomic ratios between Li, Ni, Co, and Mn were confirmed using ICP-MS (ICP-MS 7700S, Agilent). The crystal structures and particle morphologies were characterized using SEM (SU8230, Hitachi) and field-emission TEM (FE-TEM; JEM 2100F, JEOL) at the Korea Basic Science Institute (KBSI). The valence state of Ni and Co were analyzed by using XAS measurements. Ni and Co L-edge (K-edge) XAS spectra were obtained in the total electron yield (transmission yield) method at 6A (L-edge) and 1D (K-edge) beamline of the Pohang Light Source (PLS) in the Pohang Accelerator Laboratory (PAL). TOF-SIMS (TOF-SIMS5, ION-TOF GmbH) was used for chemical analysis of the surface. A pulsed 40 keV Bi<sup>+</sup> ion beam set in high-current bunched mode was used, and the analyzed area was 40 × 40 μm. All the detected secondary ions of interest possessed negative polarity. The elemental analysis of the cycled Li metal counter electrode was performed by SEM-EDS at the accelerating voltage of 20 kV with the representative area of 150 × 100 μm.

**Electrochemical Analyses of LiNi<sub>0.895</sub>Co<sub>0.085</sub>Mn<sub>0.02</sub>O<sub>2</sub>:** The electrodes were prepared using LiNi<sub>0.895</sub>Co<sub>0.085</sub>Mn<sub>0.02</sub>O<sub>2</sub> Super P and polyvinylidene fluoride (PVDF) binder in a mass ratio of 8:1:1 in *N*-methyl-2-pyrrolidone (99.5%, Aldrich). The resulting slurry was pasted onto an aluminum foil with 250 μm thickness. After being vacuum-dried at 120 °C, the electrode was pressed using a roll-press machine. Coin-type half cells (CR2032, Wellcos) were assembled using the electrode, a lithium metal counter electrode, a glass microfiber filter (grade GF/F, Whatman) as a separator, and 1 M LiPF<sub>6</sub> in ethylene carbonate/dimethyl carbonate (EC/DMC, 1:1 v/v, PanaXEtac) as the electrolyte. The preparation was performed in an Ar-filled glovebox. Galvanostatic measurements of the LiNi<sub>0.895</sub>Co<sub>0.085</sub>Mn<sub>0.02</sub>O<sub>2</sub> electrode samples were conducted in voltage ranges of 2.5–4.25 V, 2.5–4.6 V, and 2.5–4.9 V versus Li<sup>+</sup>/Li with a constant current of 40 mA g<sup>-1</sup> equivalent to 0.15 C-rate at 25 °C (WBCS 3000, WonA Tech). Ex situ electrode samples were prepared by electrochemical cycling using the coin cells. All the cycled electrode samples were rinsed with DMC and dried in an Ar-filled glovebox. EIS data were collected by charging/discharging the cells to each cut-off voltage after the 1st, 10th, 20th, and 30th cycles in the frequency range of 1 MHz to 1 mHz (ZIVE SP1, WonA Tech).

## Supporting Information

Supporting Information is available from the Wiley Online Library or from the author.

## Acknowledgements

This work was supported by the National Research Foundation of Korea (NRF) funded by the Ministry of Science and ICT (NRF-2017M2A2A6A05017652, NRF-2018M2A2B3A05074602 and NRF-2017M1A2A2044484).

## Conflict of Interest

The authors declare no conflict of interest.

## Keywords

cathodes, high voltages, Li-ion batteries, Ni-rich NCM, surface stabilization

Received: February 10, 2020

Revised: March 22, 2020

Published online: May 4, 2020

- 
- [1] M. Armand, J.-M. Tarascon, *Nature* **2008**, 451, 652.
- [2] S. Chu, Y. Cui, N. Liu, *Nat. Mater.* **2017**, 16, 16.
- [3] K. Kang, Y. S. Meng, J. Bréger, C. P. Grey, G. Ceder, *Science* **2006**, 311, 977.
- [4] D. Larcher, J.-M. Tarascon, *Nat. Chem.* **2015**, 7, 19.
- [5] V. Etacheri, R. Marom, R. Elazari, G. Salitra, D. Aurbach, *Energy Environ. Sci.* **2011**, 4, 3243.
- [6] J. N. Reimers, J. Dahn, *J. Electrochem. Soc.* **1992**, 139, 2091.
- [7] A. R. Armstrong, P. G. Bruce, *Nature* **1996**, 381, 499.
- [8] A. Rougier, P. Gravereau, C. Delmas, *J. Electrochem. Soc.* **1996**, 143, 1168.
- [9] B. Kang, G. Ceder, *Nature* **2009**, 458, 190.
- [10] J.-H. Cho, J.-H. Park, M.-H. Lee, H.-K. Song, S.-Y. Lee, *Energy Environ. Sci.* **2012**, 5, 7124.
- [11] W.-S. Yoon, M. Balasubramanian, K. Y. Chung, X.-Q. Yang, J. McBreen, C. P. Grey, D. A. Fischer, *J. Am. Chem. Soc.* **2005**, 127, 17479.
- [12] S.-M. Bak, E. Hu, Y. Zhou, X. Yu, S. D. Senanayake, S.-J. Cho, K.-B. Kim, K. Y. Chung, X.-Q. Yang, K.-W. Nam, *ACS Appl. Mater. Interfaces* **2014**, 6, 22594.
- [13] S.-T. Myung, F. Maglia, K.-J. Park, C. S. Yoon, P. Lamp, S.-J. Kim, Y.-K. Sun, *ACS Energy Lett.* **2017**, 2, 196.
- [14] A. Manthiram, J. C. Knight, S. T. Myung, S. M. Oh, Y. K. Sun, *Adv. Energy Mater.* **2016**, 6, 1501010.
- [15] H.-H. Sun, A. Manthiram, *Chem. Mater.* **2017**, 29, 8486.
- [16] F. Schipper, E. M. Erickson, C. Erk, J.-Y. Shin, F. F. Chesneau, D. Aurbach, *J. Electrochem. Soc.* **2017**, 164, A6220.
- [17] S. K. Jung, H. Gwon, J. Hong, K. Y. Park, D. H. Seo, H. Kim, J. Hyun, W. Yang, K. Kang, *Adv. Energy Mater.* **2014**, 4, 1300787.
- [18] M. Guilmard, A. Rougier, M. Grüne, L. Croguennec, C. Delmas, *J. Power Sources* **2003**, 115, 305.
- [19] R. Jung, M. Metzger, F. Maglia, C. Stinner, H. A. Gasteiger, *J. Electrochem. Soc.* **2017**, 164, A1361.
- [20] B. Strehle, K. Kleiner, R. Jung, F. Chesneau, M. Mendez, H. A. Gasteiger, M. Piana, *J. Electrochem. Soc.* **2017**, 164, A400.
- [21] R. Jung, M. Metzger, F. Maglia, C. Stinner, H. A. Gasteiger, *J. Phys. Chem. Lett.* **2017**, 8, 4820.
- [22] J. Wandt, A. T. Freiberg, A. Ogrodnik, H. A. Gasteiger, *Mater. Today* **2018**, 21, 825.
- [23] R. Jung, F. Linsenmann, R. Thomas, J. Wandt, S. Solchenbach, F. Maglia, C. Stinner, M. Tromp, H. A. Gasteiger, *J. Electrochem. Soc.* **2019**, 166, A378.
- [24] C. S. Yoon, H.-H. Ryu, G.-T. Park, J.-H. Kim, K.-H. Kim, Y.-K. Sun, *J. Mater. Chem. A* **2018**, 6, 4126.
- [25] W. Zhao, J. Zheng, L. Zou, H. Jia, B. Liu, H. Wang, M. H. Engelhard, C. Wang, W. Xu, Y. Yang, *Adv. Energy Mater.* **2018**, 8, 1800297.
- [26] H.-H. Ryu, K.-J. Park, C. S. Yoon, Y.-K. Sun, *Chem. Mater.* **2018**, 30, 1155.
- [27] M. Guilmard, L. Croguennec, C. Delmas, *J. Electrochem. Soc.* **2003**, 150, A1287.
- [28] Y. Shi, M. Zhang, D. Qian, Y. S. Meng, *Electrochim. Acta* **2016**, 203, 154.
- [29] Y. Mao, X. Wang, S. Xia, K. Zhang, C. Wei, S. Bak, Z. Shadike, X. Liu, Y. Yang, R. Xu, *Adv. Funct. Mater.* **2019**, 29, 1900247.
- [30] Y.-K. Sun, S.-T. Myung, B.-C. Park, J. Prakash, I. Belharouak, K. Amine, *Nat. Mater.* **2009**, 8, 320.
- [31] C. Grey, J. Tarascon, *Nat. Mater.* **2017**, 16, 45.
- [32] S.-W. Lee, M.-S. Kim, J. H. Jeong, D.-H. Kim, K. Y. Chung, K. C. Roh, K.-B. Kim, *J. Power Sources* **2017**, 360, 206.
- [33] W. M. Seong, K. Yoon, M. H. Lee, S.-K. Jung, K. Kang, *Nano Lett.* **2019**, 19, 29.
- [34] J. H. Lee, C. S. Yoon, J.-Y. Hwang, S.-J. Kim, F. Maglia, P. Lamp, S.-T. Myung, Y.-K. Sun, *Energy Environ. Sci.* **2016**, 9, 2152.
- [35] W. Li, J. Reimers, J. Dahn, *Solid State Ionics* **1993**, 67, 123.
- [36] H.-J. Noh, S. Yoon, C. S. Yoon, Y.-K. Sun, *J. Power Sources* **2013**, 233, 121.
- [37] A. O. Kondrakov, A. Schmidt, J. Xu, H. Geßwein, R. Mönig, P. Hartmann, H. Sommer, T. Brezesinski, J. r. Janek, *J. Phys. Chem. C* **2017**, 121, 3286.
- [38] Q. Fan, S. Yang, J. Liu, H. Liu, K. Lin, R. Liu, C. Hong, L. Liu, Y. Chen, K. An, *J. Power Sources* **2019**, 421, 91.
- [39] C. S. Yoon, D.-W. Jun, S.-T. Myung, Y.-K. Sun, *ACS Energy Lett.* **2017**, 2, 1150.
- [40] S. Schweidler, L. de Biasi, G. Garcia, A. Mazilkin, P. Hartmann, T. Brezesinski, J. r. Janek, *ACS Appl. Energy Mater.* **2019**, 2, 10, 7375.
- [41] S. Hwang, S. M. Kim, S.-M. Bak, S. Y. Kim, B.-W. Cho, K. Y. Chung, J. Y. Lee, E. A. Stach, W. Chang, *Chem. Mater.* **2015**, 27, 3927.
- [42] P. Yan, J. Zheng, J.-G. Zhang, C. Wang, *Nano Lett.* **2017**, 17, 3946.
- [43] W.-S. Yoon, O. Haas, S. Muhammad, H. Kim, W. Lee, D. Kim, D. A. Fischer, C. Jaye, X.-Q. Yang, M. Balasubramanian, *Sci. Rep.* **2015**, 4, 6827.
- [44] S. Hwang, S. M. Kim, S.-M. Bak, B.-W. Cho, K. Y. Chung, J. Y. Lee, W. Chang, E. A. Stach, *ACS Appl. Mater. Interfaces* **2014**, 6, 15140.
- [45] K. W. Nam, S. M. Bak, E. Hu, X. Yu, Y. Zhou, X. Wang, L. Wu, Y. Zhu, K. Y. Chung, X. Q. Yang, *Adv. Funct. Mater.* **2013**, 23, 1047.
- [46] S.-M. Bak, K.-W. Nam, W. Chang, X. Yu, E. Hu, S. Hwang, E. A. Stach, K.-B. Kim, K. Y. Chung, X.-Q. Yang, *Chem. Mater.* **2013**, 25, 337.
- [47] H. Konishi, M. Yoshikawa, T. Hirano, K. Hidaka, *J. Power Sources* **2014**, 254, 338.
- [48] X. Zheng, B. Zhang, P. De Luna, Y. Liang, R. Comin, O. Voznyy, L. Han, F. P. G. de Arquer, M. Liu, C. T. Dinh, *Nat. Chem.* **2018**, 10, 149.
- [49] N. Palina, L. Wang, S. Dash, X. Yu, M. B. Breese, J. Wang, A. Ruydy, *Nanoscale* **2017**, 9, 6094.
- [50] L. Mu, X. Feng, R. Kou, Y. Zhang, H. Guo, C. Tian, C. J. Sun, X. W. Du, D. Nordlund, H. L. Xin, *Adv. Energy Mater.* **2018**, 8, 1801975.
- [51] J.-H. Shim, C.-Y. Kim, S.-W. Cho, A. Missiul, J.-K. Kim, Y. J. Ahn, S. Lee, *Electrochim. Acta* **2014**, 138, 15.
- [52] J. Yang, Y. Xia, *J. Electrochem. Soc.* **2016**, 163, A2665.
- [53] D. Wang, R. Yu, X. Wang, L. Ge, X. Yang, *Sci. Rep.* **2015**, 5, 8403.
- [54] M. Wang, R. Zhang, Y. Gong, Y. Su, D. Xiang, L. Chen, Y. Chen, M. Luo, M. Chu, *Solid State Ionics* **2017**, 312, 53.
- [55] B. P. Ajayi, S. Kumari, D. Jaramillo-Cabanzo, J. Spurgeon, J. Jasinski, M. Sunkara, *J. Mater. Res.* **2016**, 31, 1596.
- [56] D. Huang, Y. Shi, A. P. Tornheim, J. Bareño, Z. Chen, Z. Zhang, A. Burrell, H. Luo, *Appl. Mater. Today* **2019**, 16, 342.
- [57] G.-L. Xu, J.-T. Li, L. Huang, W. Lin, S.-G. Sun, *Nano Energy* **2013**, 2, 394.
- [58] M. S. Kolathodi, M. Palei, T. S. Natarajan, *J. Mater. Chem. A* **2015**, 3, 7513.
- [59] J. Yang, Y. Xia, *ACS Appl. Mater. Interfaces* **2016**, 8, 1297.